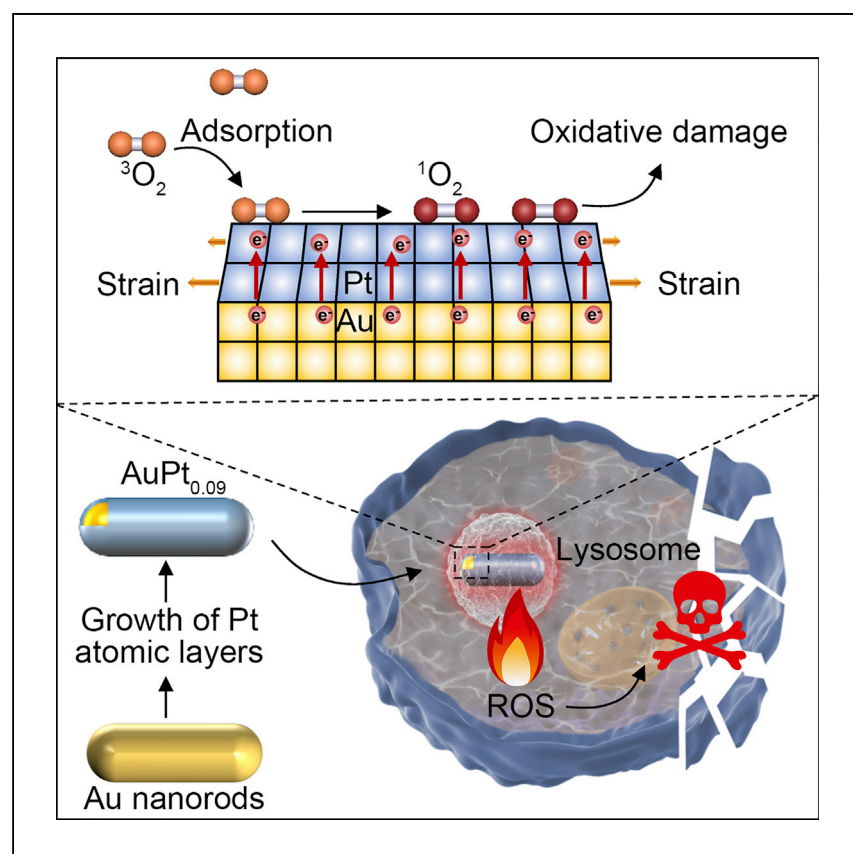## Article

A bimetallic nanocatalyst for light-free oxygen sensitization therapy

Guo et al. report a bimetallic nanocatalyst thermodynamically favoring $^3O_2$ activation into $^1O_2$ via electron-transfer-mediated spin reduction, which circumvents the limitations of current photodynamic therapy and chemodynamic therapy and which enables autocatalytic $^1O_2$ production in a light-free manner for oxygen sensitization therapy.

Xia Guo, Hongwei Liao, Jiaming Tian, ..., Liang Zhang, Fangyuan Li, Daishun Ling

lfy@zju.edu.cn (F.L.)
dsling@sjtu.edu.cn (D.L.)

Highlights

An autocatalytic bimetallic nanocatalyst for $^1O_2$ generation is synthesized

Strain and electronic effects are induced for highly efficient $^1O_2$ generation

The nanocatalyst realizes high-performance, light-free oxygen sensitization therapy

Article

A bimetallic nanocatalyst for light-free oxygen sensitization therapy

Xia Guo,[1,7] Hongwei Liao,[1,7] Jiaming Tian,[4,7] Chuang Yang,[6] Fan Xia,[1] Wenshi Liang,[1] Nan Wang,[1] Pin Li,[1] Bo Zhang,[3] Linji Gong,[3] Xi Hu,[1] Liang Zhang,[5] Fangyuan Li,[1,2,*] and Daishun Ling[1,2,3,8,*]

SUMMARY

Singlet oxygen ($^1O_2$) is extensively employed by reactive oxygen species (ROS)-based cancer therapies, such as photodynamic therapy (PDT) and chemodynamic therapy (CDT). However, the dependences of PDT on light and CDT on complex chemodynamic reactions greatly limit their $^1O_2$-generating efficiencies. Here, we exploit strain and electronic effects to fabricate a bimetallic nanocatalyst by coating a gold nanorod (AuNR) with ~2 platinum (Pt) atomic layers (AuPt$_{0.09}$), which efficiently generates $^1O_2$ from ground-state oxygen ($^3O_2$) by electron-transfer-mediated spin reduction. Density functional theory reveals strain, and electronic effects promote the adsorption of $^3O_2$ onto AuPt$_{0.09}$, which dramatically enhances $^1O_2$ generation and imparts AuPt$_{0.09}$, the highest catalytic constant ever reported for 3,3′,5,5′-tetramethylbenzidine oxidation to the best of our knowledge. With a pH-dependent catalytic activity, AuPt$_{0.09}$ realizes acidity-dependent antitumor effects both *in vitro* and *in vivo*, a proof-of-concept demonstration of autocatalytic bimetallic nanocatalyst for light-free oxygen sensitization therapy, which may open a new avenue for $^1O_2$-centered therapeutics.

INTRODUCTION

Singlet oxygen ($^1O_2$) is a type of reactive oxygen species (ROS) with a higher reactivity than the ground-state molecular oxygen ($^3O_2$), which can damage various functional biomolecules, including proteins, nucleic acids, and lipids,[1–3] leading to cell death. Therefore, $^1O_2$ can be utilized for therapeutic purposes, such as cancer treatment. Photodynamic therapy (PDT) is the most representative therapeutic modality for cancer treatment that acts by generating $^1O_2$,[4–9] but due to the limited tissue penetration of light, clinical PDT is still confined to superficial cancers, such as skin cancer[10] and bladder cancer.[11] Most recently, transition-metal-based nanoplatforms of chemodynamic therapy (CDT) have been developed to generate $^1O_2$ in a light-free manner.[12–14] However, this strategy involves tortuous chemodynamic reactions with a dependence on consuming exogenously supplied reactants for $^1O_2$ generation, which cannot maintain a high $^1O_2$-generating efficiency with the gradual depletion of the exogenous reactants. Consequently, it is appealing to develop a light-free $^1O_2$ generator that can afford sustained $^1O_2$-generating activity. Noble metal nanomaterials with intrinsic catalytic activities have shown the potential to achieve such a goal.[15–18] However, to our best knowledge, no noble-metal-based oxygen-sensitization agents reported thus far can realize tumor therapy both *in vitro* and *in vivo* due to their limited catalytic activities.[15–18] Strain and electronic effects have been reported to alter the chemisorption of the adsorbates by

[1]Institute of Pharmaceutics, College of Pharmaceutical Sciences, Zhejiang University, Hangzhou 310058, China

[2]Hangzhou Institute of Innovative Medicine, College of Pharmaceutical Sciences, Zhejiang University, Hangzhou 310058, China

[3]School of Chemistry and Chemical Engineering, Frontiers Science Center for Transformative Molecules, National Center for Translational Medicine, Shanghai Jiao Tong University, Shanghai 200240, China

[4]Department of Chemical Engineering, Tsinghua University, Beijing 100084, China

[5]School of Vehicle and Mobility, Tsinghua University, Beijing 100084, China
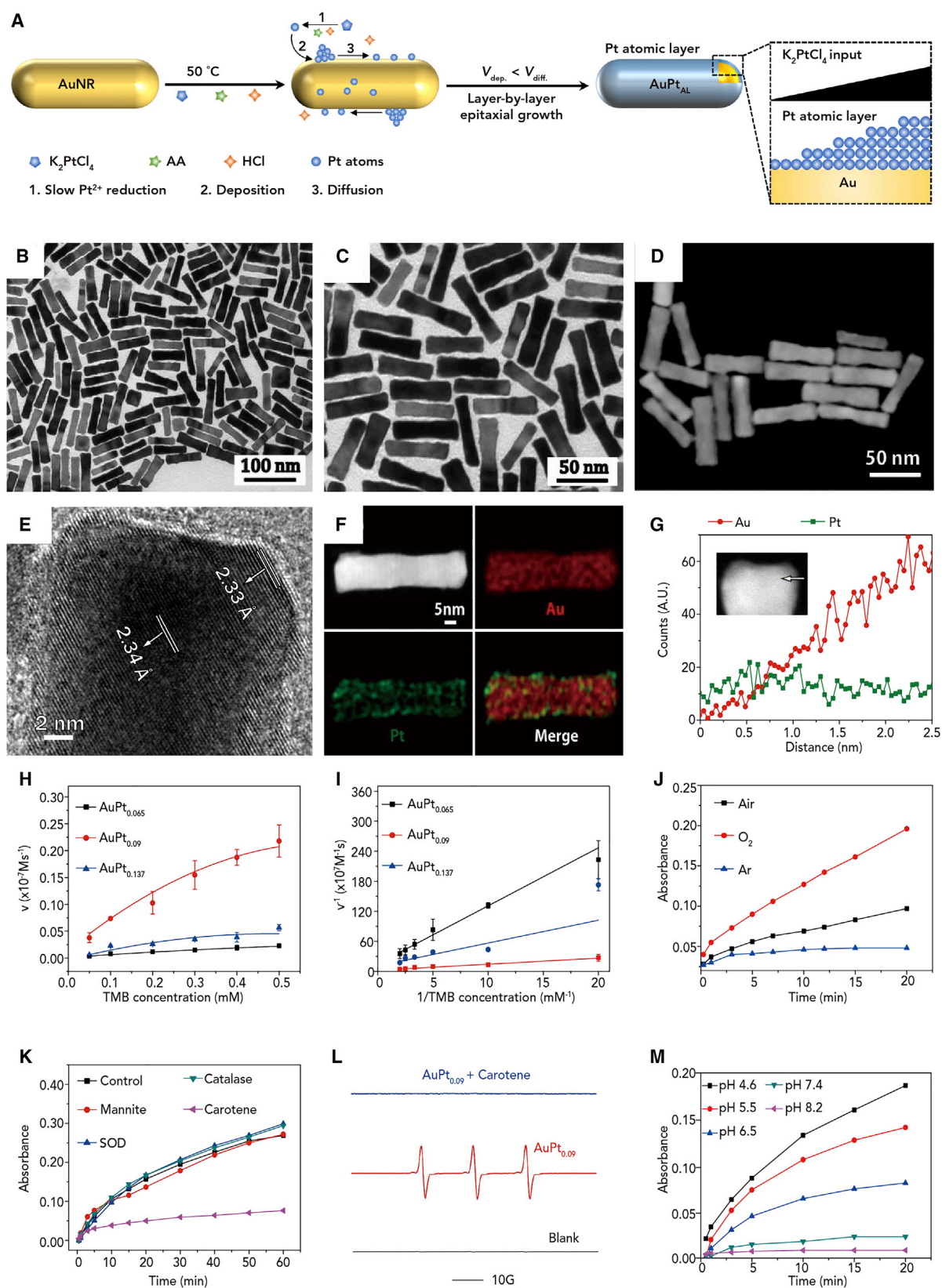
[6]Jiangsu Breast Disease Center, the First Affiliated Hospital with Nanjing Medical University, Nanjing 210029, China

[7]These authors contributed equally

[8]Lead contact

*Correspondence: lfy@zju.edu.cn (F.L.), dsling@sjtu.edu.cn (D.L.)

https://doi.org/10.1016/j.xcrp.2021.100538

modifying the electronic structures of the bimetallic surface, which in turn changes the reactivity of the adsorbates.[19–23] Hence, we hypothesize that, by leveraging the strain and electronic effects, a bimetallic nanostructure may be engineered as a superior $^1O_2$ generator for efficient tumor catalytic therapy.

To prove the concept, herein, platinum (Pt) is deposited onto the surface of gold nanorods (AuNR) as well-defined atomic layers to form the core-shell nanostructures (AuPt$_{AL}$). The electronic structure of the surface Pt is altered by the tensile strain and electron transfer induced by the AuNR core.[24,25] Experiments and density functional theory (DFT) calculations reveal the Pt shell thickness as a critical determinant to the $^1O_2$-generating activity of AuPt$_{AL}$ and present AuPt$_{0.09}$ (Pt/Au mass ratio = 0.09) with ~2 Pt atomic layers as the optimal structure for $^1O_2$ generation, which outperforms AuPt$_{0.065}$ or AuPt$_{0.137}$ that has a thinner or thicker Pt shell, respectively. AuPt$_{0.09}$ readily enters tumor cells and accumulates in lysosomes to induce cell death in a lysosomal-acidity-activated manner. Once conjugated with the arginine-glycine-aspartate (RGD) peptide to facilitate tumor uptake *in vivo*, AuPt$_{0.09}$ successfully confers potent antitumor efficacy without noticeable systemic toxicity. Such a bimetallic nanocatalyst for sustainable light-free $^1O_2$ generation and oxygen sensitization therapy may open new avenues in ROS-based tumor therapeutics.

RESULTS AND DISCUSSION

Synthesis and characterization of AuPt$_{AL}$

The monodisperse AuPt$_{AL}$ was synthesized via controlled epitaxial growth of Pt on AuNR (Figures 1A, 1B, and S1), using hydrochloric acid (HCl) to moderate the reduction of Pt precursors (K$_2$PtCl$_4$) by ascorbic acid (AA).[26,27] The energy dispersive spectroscopy (EDS) spectrum and the X-ray photoelectron spectroscopy (XPS) analysis (Figures S2A–S2C) confirm the reduction of Pt^{2+} to Pt^0 on AuNR, which exists as thin layers without forming obvious surface Pt clusters (Figures 1C and 1D). The high-resolution transmission electron microscope (HRTEM) image shows clear and continuous lattice fringes (Figure 1E) of AuPt$_{AL}$, with the lattice spacing being 2.34 Å at the body and 2.33 Å at the edge, which correspond to the crystal planes of Au(111) and Pt(111) in the X-ray diffraction (XRD) patterns (Figure S2D). Although Pt has a smaller lattice constant than Au, there is almost no decrease in the lattice spacing from the body to the edge, which results from the Au-induced tensile strain on Pt.[28,29] Moreover, the elemental mapping (Figure 1F) and line scanning analysis (Figure 1G) via energy-dispersive X-ray (EDX) spectra show that Pt uniformly distributes on the surface of AuNR, confirming the epitaxial relationship between Au and Pt. To improve the biocompatibility, AuPt$_{AL}$ is grafted with methoxy poly(ethylene glycol)-5000-thiol (mPEG$_{5000}$-SH), which is verified by the thermogravimetry analysis

Figure 1. Synthesis, characterization, and catalytic activities of AuPt$_{AL}$

(A) The synthesis route of AuPt$_{AL}$. Pt^{2+} is slowly reduced to Pt by AA under an acidic condition at 50°C, which then grows epitaxially as Pt atomic layers on the surface of AuNR because the velocity of Pt deposition ($V_{dep.}$) is slower than that of Pt diffusion ($V_{diff.}$). By varying the input of K$_2$PtCl$_4$ during synthesis, AuPt$_{AL}$ with different Pt shell thicknesses can be obtained.

(B–D) The shape and dispersibility and AuPt$_{AL}$ as shown in (B and C) TEM images and (D) the high-angle annular dark-field scanning transmission electron microscopy (HAADF-STEM) image.

(E and F) The epitaxial relationship between Au and Pt shown in the (E) HRTEM image and (F) EDX elemental mapping of AuPt$_{AL}$.
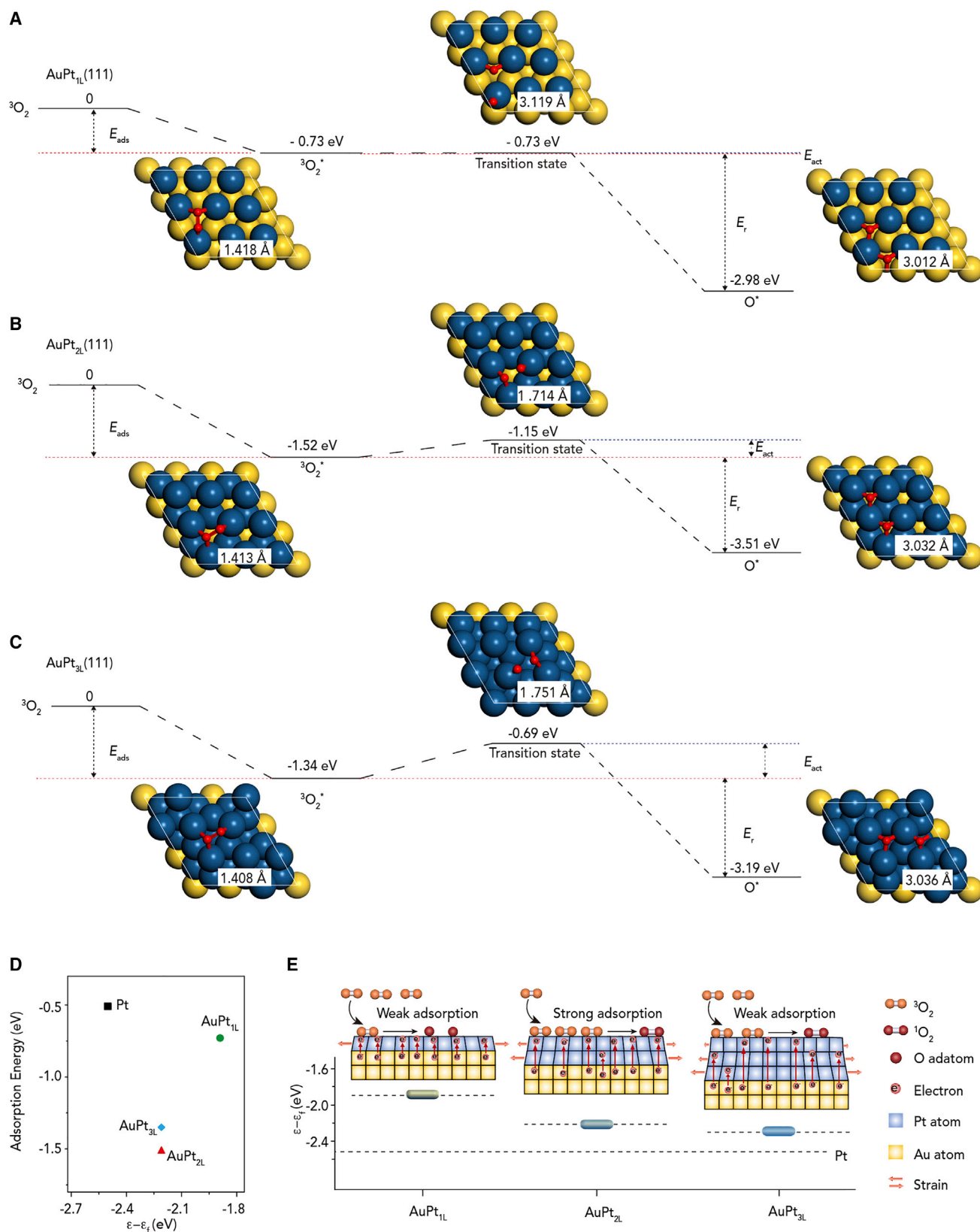
(G) The EDX line-scanning analysis of AuPt$_{AL}$ along the white arrow (inset) indicating the Pt shell as ultrathin atomic layers.

(H and I) The catalytic activities of PEGylated AuPt$_{0.065}$, AuPt$_{0.09}$, or AuPt$_{0.137}$ shown by the (H) Michaelis-Menten curves and (I) double-reciprocal plots for TMB oxidation. Data are presented as means ± SD, n = 3.

(J and K) The absorbance of TMB at 650 nm upon oxidation catalyzed by PEGylated AuPt$_{0.09}$ under (J) different atmospheres and (K) in the presence of different ROS quenchers.

(L) ESR spectra of TEMP upon oxidation catalyzed by PEGylated AuPt$_{0.09}$ with or without carotene.

(M) The absorbance of TMB at 650 nm upon oxidation catalyzed by PEGylated AuPt$_{0.09}$ under different pH conditions.

A AuPt$_{1L}$(111)

$^3O_2$ 0

E_{ads}

3.119 Å

− 0.73 eV

$^3O_2^*$

− 0.73 eV

Transition state

E_{act}

E_r

-2.98 eV

O*

1.418 Å

3.012 Å

B AuPt$_{2L}$(111)

$^3O_2$ 0

E_{ads}

1.714 Å

-1.52 eV

$^3O_2^*$

-1.15 eV

Transition state

E_{act}^*

E_r

-3.51 eV

O*

1.413 Å

3.032 Å

C AuPt$_{3L}$(111)

$^3O_2$ 0

E_{ads}

1.751 Å

-1.34 eV

$^3O_2^*$

-0.69 eV

Transition state

E_{act}

E_r

-3.19 eV

O*

1.408 Å

3.036 Å

D

Adsorption Energy (eV)

Pt

AuPt$_{1L}$

AuPt$_{3L}$

AuPt$_{2L}$

$\varepsilon - \varepsilon_f$ (eV)

E

$^3O_2$

Weak adsorption   Strong adsorption   Weak adsorption

$\varepsilon - \varepsilon_f$ (eV)

AuPt$_{1L}$ AuPt$_{2L}$ AuPt$_{3L}$

Pt

$^3O_2$
$^1O_2$
O adatom
Electron
Pt atom
Au atom
Strain

(TGA) (Figure S3A). Typically, the PEGylated AuPt$_{AL}$ has a hydrodynamic size of ~73 nm and a negative surface charge of ~10 mV (Figures S3B and S3C).

The Pt shell thickness determines the $^1O_2$-generating activity of AuPt$_{AL}$

Because the strain and electronic effects act only at the atomic scale,[30–33] the Pt shell thickness can dramatically affect the catalytic activity of AuPt$_{AL}$. To investigate the structure-activity relationship, AuPt$_{AL}$ with different Pt thicknesses were prepared by varying the amount of Pt precursors during the synthesis. Among the PEGylated AuPt$_{AL}$ with different Pt/Au mass ratios (0.065, 0.09, and 0.137; Figures 1A and S4), AuPt$_{0.09}$ exhibits the highest catalytic activity in 3,3′,5,5′-tetramethylbenzidine (TMB) oxidation assay, as revealed by the Michaelis-Menten curves and the double-reciprocal plots showing the kinetic parameters (Figures 1H and 1I). In fact, AuPt$_{0.09}$ possesses a catalytic constant (kcat) of 3.9×10^3 S^{-1}, which is 13.7 times higher than that of AuPt$_{0.065}$ and 2.5 times higher than that of AuPt$_{0.137}$, respectively (Table S1). To our best knowledge, this is the highest kcat ever reported for nanoparticle-catalyzed TMB oxidation (Table S2).[34–37] Notably, AuPt$_{0.09}$-catalyzed TMB oxidation shows evident oxygen dependence (Figure 1J) and can only be inhibited by the specific $^1O_2$ quencher carotene (Figure 1K), indicating $^1O_2$ as the active species generated by AuPt$_{0.09}$, which is further corroborated by the characteristic 1:1:1 electron spin resonance (ESR) signal of 2,6,6,6-tetramethylpiperidon (TEMP) oxidation (Figure 1L).[17] Moreover, AuNR or Pt nanoparticles (PtNP) have much lower $^1O_2$-generating activity than AuPt$_{0.09}$ (Figure S5), underlining the critical role of the bimetallic surface in enhancing the catalytic activity. Interestingly, the $^1O_2$-generating activity of AuPt$_{0.09}$ shows a strong dependence on the acidic pH (Figures 1M and S6), likely due to the $^1O_2$-scavenging ability of noble metal nanomaterials under neutral and basic conditions.[38–40]

To investigate the mechanism underlying the striking catalytic activity of AuPt$_{0.09}$, DFT calculations were performed to characterize the process of $^3O_2$ activation on (111) surfaces of AuPt$_{AL}$. From the EDX line-scanning spectra (Figure 1G) of AuPt$_{0.09}$ and its size increment compared with AuNR (~1.1 nm in diameter; Figure S7), the average number of Pt atomic layers on AuPt$_{0.09}$ is estimated to be 2. Hence, we modeled Au slabs covered by 1, 2, or 3 Pt atomic layers (namely AuPt$_{1L}$, AuPt$_{2L}$, and AuPt$_{3L}$, respectively) to simulate how the Pt shell thickness would affect the $^1O_2$ generation. Interestingly, compared with pure Au and Pt surfaces, AuPt$_{1L}$, AuPt$_{2L}$, and AuPt$_{3L}$ surfaces all have much lower $^3O_2$ adsorption energies under the most favorable top-fcc-bridge configuration (Figures 2A–2C and S8), which confer stronger adsorption affinities for $^3O_2$. This result is attributed to the combined tensile strain and electronic effects on the Pt shell,[31,41] which causes an upshift of the d band center (ε_d) of the surface Pt, favoring oxygen-metal bonding (Figure 2D).[20,42] Notably, AuPt$_{1L}$ has a higher ε_d compared with AuPt$_{2L}$ or AuPt$_{3L}$ but exhibits a weaker $^3O_2$ adsorption, which reflects the well-documented complexity of the chemisorption kinetics on a metal monolayer supported by another metal substrate.[43] Moreover, it is thermodynamically more favorable for adsorbed $^3O_2$ molecules to dissociate into O adatoms on AuPt$_{1L}$ than on AuPt$_{2L}$ or on AuPt$_{3L}$ (Figures 2A–2C), leading to lower overall production of $^1O_2$ on AuPt$_{1L}$ than on AuPt$_{2L}$ or AuPt$_{3L}$.

Figure 2. Simulation data for the $^1O_2$-generating activities of AuPt$_{AL}$ with different number of Pt atomic layers

(A–C) Calculated activation energies (in eV) for $^3O_2$ adsorption and dissociation on (A) AuPt$_{1L}$(111), (B) AuPt$_{2L}$(111), and (C) AuPt$_{3L}$(111). E_{ads}, adsorption energy; E_{act}, activation energy; E_r, reaction energy. The O−O atomic distances (in Å) of adsorbed oxygen molecules (red) are annotated above the AuPt slabs.

(D) The relationship between the $^3O_2$ adsorption energy and the d-band center (ε_d-ε_f, relative to the Fermi level) of the (111) facet of simulated Pt, AuPt$_{1L}$, AuPt$_{2L}$, or AuPt$_{3L}$.

(E) Schematic illustration of the combined effects of the strain and the electron transfer on $^1O_2$ production on AuPt$_{1L}$, AuPt$_{2L}$, or AuPt$_{3L}$.
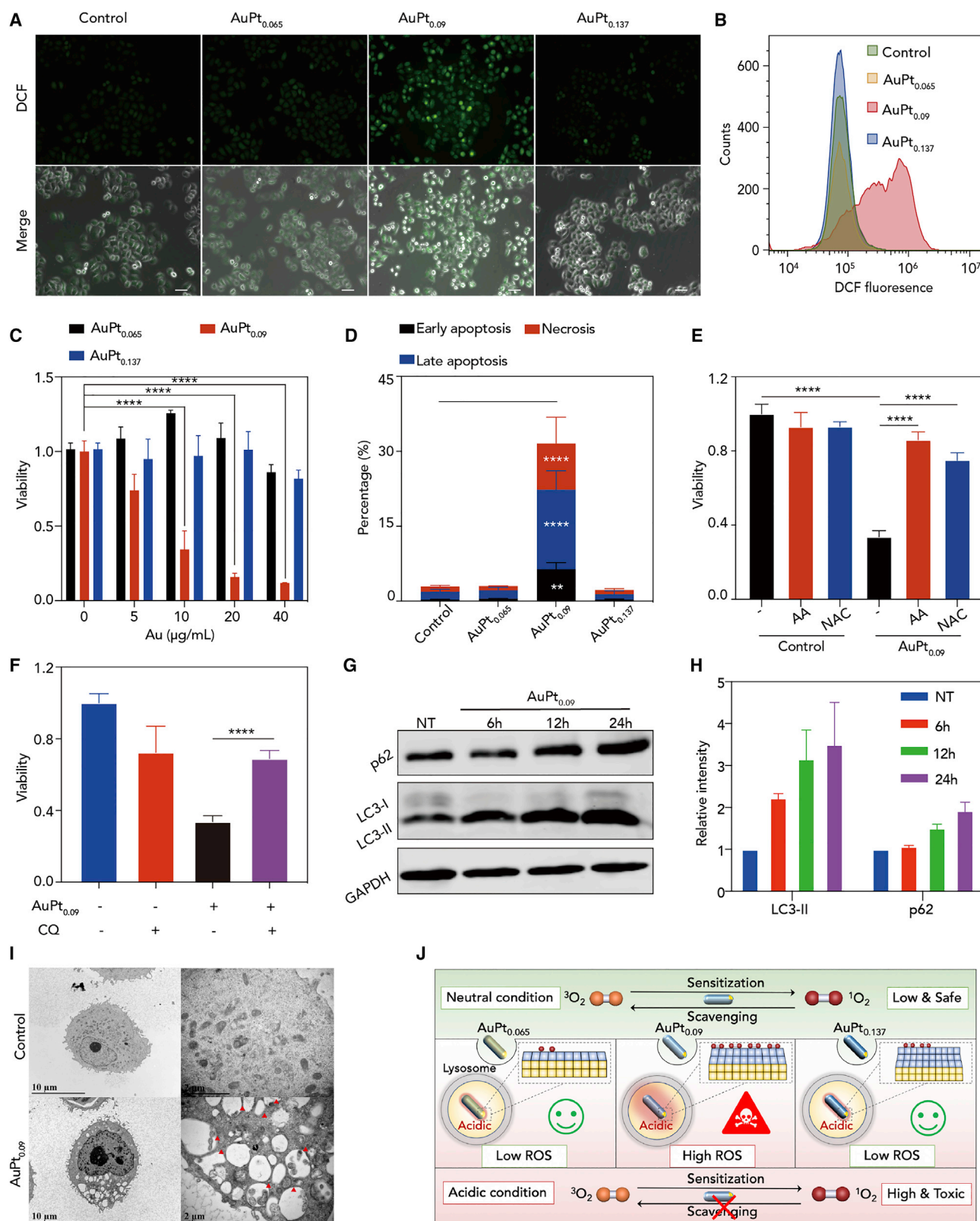
We further calculated the projected density of states (PDOS) and spin charge density (SCD) of adsorbed $^3O_2$ molecules to characterize their spin reduction caused by electron transfer. Regardless of the Pt layer number, Au-supported Pt effectively induces a spin reduction of $^3O_2$ by transferring ~0.65 electron charge to the antibonding π^* orbital of $^3O_2$ (Figures S9 and S10).[17,18,44,45] Collectively, we conclude that fewer Pt atomic layers, except the monolayer Pt, impart higher $^1O_2$-generating activities, mainly by imparting stronger chemisorption of $^3O_2$ (Figure 2E). Notably, although the activated $^3O_2$ on the surface of $AuPt_{AL}$ surface acts like $^1O_2$ in oxidative reactions, such ROS activated by electron transfer is different from the well-defined singlet oxygen with a spin flip after energy transfer from conventional molecular photosensitizers. In a typical type II mechanism of photosensitization, there are two electrons with antiparallel spins in the antibonding π^* orbital of the excited oxygen molecules, resulting in a total spin quantum number of 0 and a singlet spin state.[46,47] In contrast, during oxygen sensitization catalyzed by $AuPt_{AL}$, the total spin quantum number is not reduced by a spin flip but by the electron transfer from the metal surface to the antibonding π^* orbital of oxygen molecules.[17,18] Apparently, in both cases, the altered spin state of the activated oxygen molecules will permit spin-allowed reactions, conferring higher reactivity toward organic molecules. Of note, because oxygen sensitization mediated by electron-transfer-induced spin reduction does not require an exogenous energy source, it can overcome the major obstacle in conventional light-dependent photosensitization, which is the limited penetration depth of light.

$AuPt_{0.09}$ with ~2 Pt atomic layers effectively kills tumor cells *in vitro* and *in vivo*

Next, the antitumor effects of $AuPt_{0.065}$, $AuPt_{0.09}$, and $AuPt_{0.137}$ were examined *in vitro* and *in vivo*. The PEGylated $AuPt_{0.065}$, $AuPt_{0.09}$, and $AuPt_{0.137}$ all have high colloidal stability in water or serum-containing medium for up to 14 days (Figure S11). They all readily enter tumor cells with comparable cellular uptake efficiencies and share the identical subcellular accumulation in acidic late endosomes and lysosomes, as visualized by fluorescent imaging and TEM imaging (Figure S12). However, only $AuPt_{0.09}$ induces intense intracellular ROS, exhibiting much higher cytotoxicity in comparison with $AuPt_{0.065}$ or $AuPt_{0.137}$ and with pure AuNR and Pt nanoparticles (Figures 3A–3D and S13), which corroborates the indispensable role of the unique bimetallic structure in conferring efficient catalytic activities. The cytotoxicity of $AuPt_{0.09}$ is unlikely to be induced by Pt ions leached from the Pt atomic layer, because $AuPt_{0.09}$ remains chemically stable without significant release of free Pt ions even under an acidic condition (Figure S14). Notably, the cytotoxicity

Figure 3. Oxygen-sensitization-mediated cytotoxicity of PEGylated $AuPt_{0.065}$, $AuPt_{0.09}$, and $AuPt_{0.137}$

(A and B) Microscopy (A) and flow cytometry analysis (B) of intracellular ROS indicated by dichloro-dihydro-fluorescein diacetate (DCFH-DA) staining after different treatments for 12 h. Scale bar in (A), 50 μm.

(C) Cell viability after different treatments for 24 h. Data are presented as means ± standard deviation (SD); n ≥ 3; ****p < 0.0001; two-way ANOVA.

(D) Apoptosis determined by flow cytometry analysis of annexin V and propidium staining after different treatments (10 μg/mL Au) for 24 h. Data are presented as means ± SD; n = 3; ****p < 0.0001; **p < 0.01; two-way ANOVA.

(E) Cell viability after treatments with PEGylated $AuPt_{0.09}$ for 24 h in the absence or presence of AA (200 μM) or N-acetylcysteine (NAC) (2 mM). Data are presented as means ± SD; n ≥ 4; ****p < 0.0001; one-way ANOVA.

(F) Cell viability after indicated treatments for 24 h. CQ (chloroquine) (25 μM), a lysosome acidification inhibitor, is shown. Data are presented as means ± SD; n = 4; ****p < 0.0001; one-way ANOVA.

(G) The protein levels of p62 and LC3 after treatment with $AuPt_{0.09}$ (10 μg/mL Au) for different periods of time. GAPDH is used as a loading control.

(H) Semi-quantification of (F). Data are means ± SD; n = 3.

(I) TEM images of cells treated with or without $AuPt_{0.09}$ (10 μg/mL Au) for 12 h. Red arrows indicate accumulated autophagic vacuoles.

(J) Schematic illustration of the impacts of the Pt shell thickness and the environmental acidity on $^1O_2$-generating activities of $AuPt_{0.065}$, $AuPt_{0.09}$, and $AuPt_{0.137}$. $AuPt_{0.09}$ has the optimal structure to generate the highest level of $^1O_2$ and thus the strongest cytotoxicity but only under acidic conditions, likely due to the $^1O_2$-scavenging activity of noble metal nanomaterials under neutral conditions.
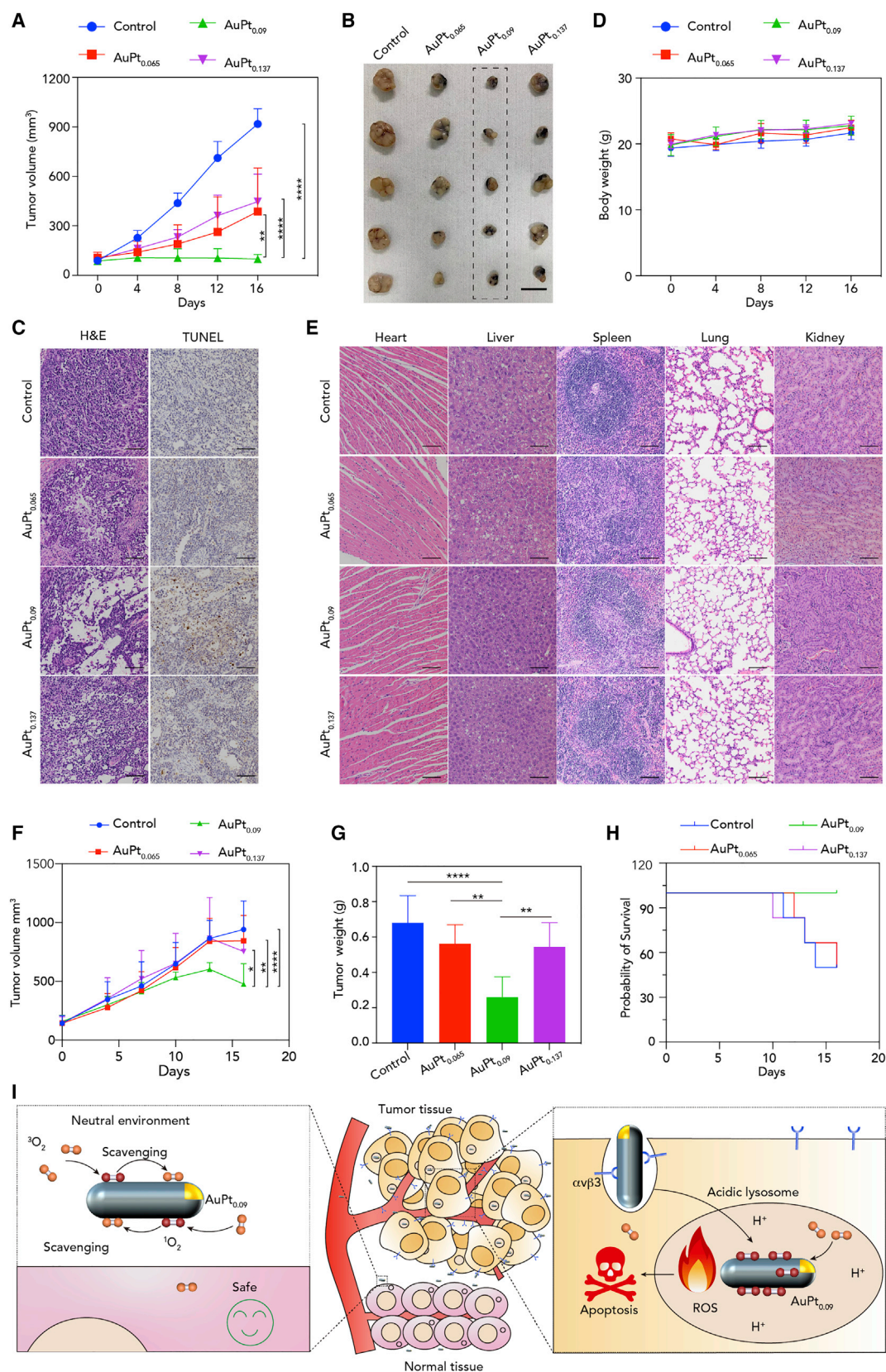
of $AuPt_{0.09}$ can be countervailed by antioxidants, including AA and N-acetylcysteine (NAC) (Figure 3E), indicating the ROS-dependent mechanism of action. Furthermore, the lysosome acidification inhibitor chloroquine protects against $AuPt_{0.09}$-induced cytotoxicity (Figure 3F), manifesting the indispensable role of lysosome acidity in $AuPt_{0.09}$-induced oxygen sensitization. Interestingly, $AuPt_{0.09}$ treatment significantly impairs the execution of autophagy, as shown by the increased protein levels of autophagic flux-related p62 and LC3-II and by the abnormal accumulation of autophagic vacuoles (Figures 3G–3I). Collectively, these results demonstrate that the optimal Pt shell thickness and the environmental acidity are both crucial to $AuPt_{0.09}$ in generating sufficient $^1O_2$ and thus substantial cytotoxicity (Figure 3J).

The pH-dependent catalytic activity of $AuPt_{0.09}$ is anticipated to harness the physiological pH gradient as a natural barrier to exert antitumor effects while minimizing systemic toxicity *in vivo*. To facilitate tumor accumulation and uptake by tumor cells *in vivo*, the PEGylated $AuPt_{0.065}$, $AuPt_{0.09}$, and $AuPt_{0.137}$ were further conjugated with RGD peptides that can bind to αvβ3 integrins expressed by tumor neovasculature cells and tumor cells,[48–52] which were verified by positively shifted zeta potentials and the Fourier transform infrared (FTIR) spectra (Figure S15). Upon intratumoral injection, $AuPt_{0.09}$ manifests significantly stronger antitumor efficacy in comparison with $AuPt_{0.065}$ or $AuPt_{0.137}$ (Figures 4A–4C), completely halting tumor growth without causing evident adverse effects (Figures 4D and 4E). Importantly, $AuPt_{0.09}$ also shows enhanced antitumor effects in comparison with $AuPt_{0.065}$ or $AuPt_{0.137}$ upon systemic administration, without causing evident systemic toxicity (Figures 4F–4H and S16), demonstrating the robustness of $AuPt_{0.09}$ against the harsh biological environment during transportation. The resistance of $AuPt_{0.09}$ to deactivation during transportation may be ascribed to several reasons. First, the PEGylation can protect against particle aggregation, opsonization, and clearance by the mononuclear phagocyte system (MPS)/reticular endothelial system (RES).[53,54] Second, the PEGylation can prolong the blood circulation time, which facilitates passive tumor targeting as well as active tumor targeting mediated by the conjugated RGD peptides.[53,55,56] Third, $AuPt_{AL}$ exhibits excellent chemical stability due to the inert nature of noble metals and the core shell structure, where the Au core can stabilize the Pt shell and protect it from dissolution by positively shifting its oxidative potential,[57] thus maintaining the crucial bimetallic structure of $AuPt_{AL}$ during transportation without inducing the dissolution of the Pt atomic layer.

Moreover, intravenous injection of $AuPt_{0.09}$ does not incur noticeable acute hematotoxicity and organ damage (Figure S17) or evident long-term toxicity (Figure S18), indicating the good biocompatibility of the RGD-modified $AuPt_{0.09}$. Such biosafety

Figure 4. *In vivo* antitumor effects and biosafety profiles of RGD-conjugated $AuPt_{0.065}$, $AuPt_{0.09}$, and $AuPt_{0.137}$

(A) Tumor growth curves of tumor-bearing nude mice treated with intratumoral injection of $AuPt_{0.065}$, $AuPt_{0.09}$, or $AuPt_{0.137}$. Data are means ± SD; n = 5. **p < 0.01; ****p < 0.0001; two-way ANOVA.

(B) Photographs of tumors dissected from tumor-bearing nude mice after termination of different treatments in (A). Scale bar, 15 mm.

(C) Hematoxylin and eosin (H&E) staining and horseradish peroxidase-3,3'-diaminobenzidine (HRP-DAB)-based terminal deoxynucleotidyl transferase dUTP nick end labeling (TUNEL) of tumors dissected from tumor-bearing nude mice after termination of different treatments in (A). Brownish staining indicates TUNEL positive. Scale bar, 100 μm.

(D) Body weights of tumor-bearing mice under different treatments in (A). Data are means ± SD; n = 5.

(E) H&E staining of organs collected from tumor-bearing mice after termination of different treatments in (A). Scale bar, 100 μm.

(F–H) The tumor growth curves (F), the tumor weights at the endpoint (G), and the survival of tumor-bearing mice (H) treated with intravenous injection of $AuPt_{0.065}$, $AuPt_{0.09}$, or $AuPt_{0.137}$. Data in (F) and (G) are means ± SD; n = 6. *p < 0.05; **p < 0.01; ****p < 0.0001; two-way ANOVA in (F); one-way ANOVA in (G).

(I) Schematic illustration of the impacts of the Pt shell thickness and the environmental acidity on $^1O_2$-generating activities of $AuPt_{0.065}$, $AuPt_{0.09}$, and $AuPt_{0.137}$. $AuPt_{0.09}$ has the optimal structure to generate the highest level of $^1O_2$ and thus the strongest cytotoxicity but only under acidic conditions, likely due to the $^1O_2$-scavenging activity of noble metal nanomaterials under neutral conditions.

of $AuPt_{0.09}$ can be ascribed to the tumor-targeting ability and acidity-dependent cytotoxicity of RGD-modified $AuPt_{0.09}$, the chemically inert nature of Au or Pt, as well as the higher tolerance of normal cells to ROS.[58] These results show that the rationally designed and surface-engineered $AuPt_{0.09}$ can exert potent antitumor effects by sustainable $^1O_2$ generation in the acidic intracellular microenvironment. In contrast, $AuPt_{0.09}$ remains safe in the neutral environment of normal tissues, likely due to the $^1O_2$-scavenging activity of noble metal nanomaterials under neutral conditions.[38–40] To this end, $AuPt_{0.09}$ has clearly shown the great potential to serve as a biocompatible and highly efficient antitumor therapeutic agent (Figure 4I).

In summary, our results show that the $AuPt_{0.09}$ with ~2 Pt atomic layers can substantially benefit from the strain and electronic effects, leading to a bimetallic nanostructure thermodynamically favorable for $^3O_2$ activation into $^1O_2$ via an electron-transfer-mediated spin reduction. This rationally designed and highly efficient bimetallic nanocatalyst, for the first time, realizes sustainable autocatalytic $^1O_2$ production for effective oxygen sensitization cancer therapy both *in vitro* and *in vivo* by exploiting the pH-dependent catalytic activities of noble metal nanomaterials, which may open a new avenue for $^1O_2$-based antitumor therapeutics. Moreover, the $AuPt_{0.09}$ can be readily modified with different targeting ligands, holding a great potential for targeted treatment of various diseases without a depth limitation, e.g., tumors, bacterial infections, and inflammatory diseases, by generating $^1O_2$ in a light-free manner. Notably, such nanocatalyst-generated ROS are surface bond, which requires the substrates to directly contact the metal surface for the oxidative reaction to occur. Hence, the surface property of the nanocatalyst, such as the hydrophobicity and hydrophilicity that will affect the access and binding of the substrates to the surface catalytic sites of the nanocatalyst, is crucial to the efficiency of the translation of the ROS production into subsequent biological effects. Further optimization of the surface ligands to facilitate the interaction of the surface-bound ROS with surrounding biomolecules would allow the full exploitation of $AuPt_{0.09}$ for desired therapeutic purposes.

EXPERIMENTAL PROCEDURES

Resource availability

Lead contact
Further information and requests for resources should be directed to and will be fullfilled by the lead contact, Prof. Daishun Ling (email: dsling@sjtu.edu.cn).

Materials availability
The materials generated in this study are available from the lead contact author upon request.

Data and code availability
The data that support the findings of this study are available from the lead contact author on request.

Chemicals and instruments
$HAuCl_4 \cdot xH_2O$ (x = ~3–5; Au ~47.8%), K_2PtCl_4 (Pt ≥ 45.0%), TMB, carotene, mannite, TEMP, sodium acetate (NaAc), and acetate were purchased from Aladdin Industrial Inc. (Shanghai, China). Cetyltrimethylammonium bromide (CTAB) (≥99%), silver nitrate (≥99.8%), sodium borohydride (≥96%), AA (≥99.7%), and HCl (~36.0%–38.0%) were purchased from Sinopharm Chemical Reagent Co., Ltd. (Shanghai, China). Superoxide dismutase (SOD) and catalase were purchased from Shanghai Yuanye Bio-Technology Co., Ltd. (Shanghai, China). All these reagents were used without any further purification.

UV visible (UV-vis) absorption spectra were recorded by using a Shimadzu UV-2450 spectrophotometer. Low-magnification TEM images were acquired with a transmission electron microscope (JEM-1010) at an accelerating voltage of 100 kV. HRTEM images and EDS spectra were collected on an analytical transmission electron microscope of FEI Tecnai G^2 F20 S-TWIN (FEI, USA) at an accelerating voltage of 200 kV. EDX mapping and line-scanning EDX spectra were acquired using an FEI Titan G^2 80-200 ChemiSTEM (FEI, USA). XRD pattern was collected on an X-pert Powder (PANalytical B.V., Holland). Zeta potential measurements were performed on a Nano ZS instrument (Malvern, UK). XPS analysis was performed on a VG Scientific ESCALAB Mark II spectrometer. The contents of Au and Pt in the product were determined by using a PerkinElmer NexION 300X inductively coupled plasma mass spectrometer (ICP-MS). ESR spectrum was measured by using the Bruker A300 EPR spectrometer.

Synthesis of AuPt$_{AL}$

High-quality AuNRs were prepared via a modified seed-mediated growth process.[59] In brief, 0.5 mL of 10 mM HAuCl$_4$, 0.1 mL of 10 mM AgNO$_3$, 0.2 mL of 1 M HCl, 80 μL of 0.1 M AA, and 30 μL of seeds were added into 10 mL of 0.1 M CTAB. The solution was stirred for 30 s and left still at 27°C for 12 h. The obtained AuNRs were purified twice by centrifugation at 8,000 rpm for 20 min and then dispersed in deionized water to make the AuNR stock solution with a final particle concentration of 0.8 nM. For the synthesis of AuPt$_{0.09}$, 1.05 mL of 0.2 M CTAB, 250 μL of 10 mM K$_2$PtCl$_4$, 200 μL of 1 M HCl, and 50 μL of 100 mM AA were added into 20 mL of AuNR stock solution. The solution was stirred for 30 s and left still at 50°C for 5 h. The AuPt$_{AL}$ with different Pt contents were obtained following a similar procedure except for the amounts of K$_2$PtCl$_4$ and AA (AuPt$_{0.065}$, 125 μL of 10 mM K$_2$PtCl$_4$, 25 μL of 100 mM AA; AuPt$_{0.137}$, 500 μL of 10 mM K$_2$PtCl$_4$, 100 μL of 100 mM AA). The products were collected by centrifugation, washed, and then dispersed in deionized water for further characterization.

PEGylation of AuPt$_{AL}$

In brief, 10 mg of mPEG$_{5000}$-SH and 1 mg of AuPt$_{AL}$ were mixed in 10 mL deionized water with magnetic stirring for 24 h at room temperature (RT) in darkness. Finally, the PEGylated-AuPt$_{AL}$ was purified three times by centrifugation at 8,000 rpm for 20 min and then dispersed in deionized water for further use. For RGD conjugation, 1 mg of AuPt$_{AL}$ was mixed with 10 mg of NH$_2$-PEG$_{5000}$-SH in 10 mL deionized water with magnetic stirring and kept for 24 h at RT in darkness. Finally, the PEGylated-AuPt$_{AL}$ was purified three times by centrifugation at 8,000 rpm for 20 min and then dispersed in 10 mL deionized water. To activate the carboxyl groups of RGD, 10 mg of 1-ethyl-3-(—3-dimethylaminopropyl) carbodiimide hydrochloride (EDC) and 2.5 mg of N-hydroxysuccinimide (NHS) were dissolved in 10 mL phosphate-buffered saline (PBS) (100 mM) solution (pH 6.0) and then 100 μL of the RGD stock solution (50 mg/mL) was added into the solution to react for 20 min. The activation solution was then mixed with the AuPt$_{AL}$ for the conjugation reaction. After 24 h, RGD-conjugated AuPt$_{AL}$ was collected by centrifugation at 8,000 rpm for 20 min and then dialyzed against deionized water for 24 h. The final product was collected by centrifugation at 8,000 rpm for 20 min and re-dispersed in ~500 μL sterilized deionized water.

TMB measurement

10 μL of PEGylated AuPt$_{AL}$ was added to 2 mL of 0.2 M acetic acid (HAc)/NaAc buffer solution (pH 4.6; final concentration of Pt is 1 μg/mL), and the solution was stirred for 2 min at RT. Then, 20 μL of 50 mM TMB aqueous solution was added to start the oxidizing reaction of TMB at RT. The oxidation process of TMB was recorded by measuring the absorption spectra of the solution at different time points. The

measurements were carried out in various gas environments to evaluate the activation properties of molecular oxygen. Different scavenger molecules (carotene, 2 mg; mannite, 50 mM, 100 μL; catalase, 4,000 units/mL, 100 μL; superoxide dismutase, 4,000 units/mL, 100 μL) were added into the solution to verify the type of active oxygen species.

The reaction kinetics assay was carried out at RT in 0.2 M HAc/NaAc solution (pH 4.6). The absorption spectra of TMB were recorded at a 15-s interval for a total of 10 min. The apparent kinetic parameters were calculated using the Michaelis-Menten equation $v = V_{max} \times [S]/(K_m+[S])$, where V_{max} represents the maximum reaction velocity, [S] is the concentration of substrate, and K_m is the Michaelis constant.

ESR measurements

For $^1O_2$ detection, 10 μL of aqueous suspension of samples (final concentration is 20 μg/mL of Au/1.8 μg/mL of Pt) and 40 μL of 1 M TEMP aqueous solution were added to 100 μL of 0.2 M HAc/NaAc solution (pH 4.6, 6.5, and 7.4). TEMP was used as the singlet oxygen-trapping agent for detecting the singlet oxygen generation. After 5 min of incubation at RT, the mixture was transferred to a quartz capillary tube and placed in the ESR cavity for measurement.

Computational methods

Vienna *ab initio* simulation (VASP) package was used to perform spin-polarized DFT calculations. The frozen-core all-electron projector augmented wave (PAW) method was used to describe electron-ion interaction during the calculation, with the generalized gradient approximation with the Perdew-Burke-Ernzerhof (PBE) functional for exchange-correlation energy. An energy cutoff of 400 eV was used for the plane-wave expansion of the electronic wave function. Pure Au and Pt surfaces were modeled as 3×3 atomic slabs with four layers. As for $AuPt_{AL}$, surfaces were modeled in the same size, and 1–3 layers of Pt atoms were placed above four Au substrate layers. The vacuum region was set to 25 Å to avoid interaction between surfaces. The bottom two layers were fixed to the bulk positions during the relaxation. In the relaxation, the force convergence criterion was set to 0.03 eV/Å, and the energy convergence criterion was 10^{-4} eV. The first Brillouin zone was sampled with $3 \times 3 \times 1$ k-points using the Monkhorst-Pack method. The "climbing images" nudged elastic band (CI-NEB) algorithm was employed to search for transition states (TSs). For the search of TSs, the same force threshold as the geometrical optimization was used.

Cell culture

Human hepatocarcinoma cells (Huh-7) were purchased from National Collection of Authenticated Cell Cultures (National Science & Technology Infrastructure) and cultured in Dulbecco's modified eagle's medium (DMEM) supplemented with 10% fetal bovine serum and 1% penicillin/streptomycin. Cells were maintained in a humidified incubator at 37°C under an atmosphere containing 5% CO_2.

DCFH-DA staining and detection

Huh-7 cells grown in 12-well plates were incubated with $AuPt_{0.065}$, $AuPt_{0.09}$, or $AuPt_{0.137}$ of the same concentration in terms of Au mass (10 μg/mL) for 12 h, followed by the removal of culture medium and wash with DMEM twice. The cells were then incubated with 500 μL DMEM containing 1 μM DCFH-DA (Nanjing Jiancheng) for 10 min and subsequently washed with PBS (pH 7.4). For microscopic examination, the cells were kept in PBS and imaged on a Nikon Ti microscope using the phase contrast and the fluorescein isothiocyanate (FITC) channels under a 20× objective. For flow cytometry analysis, the cells were trypsinized, centrifuged (6,000 rpm,

5 min), and resuspended in 300 μL PBS. The fluorescence of DCFH-DA was then detected using flow cytometry (Cytoflex, Beckman) using the FITC channel, with at least 10,000 cells recorded for each sample.

Pt ion release

500 μg of $AuPt_{AL}$ (in terms of Au) in 1 mL deionized water was sealed in a dialysis bag with a molecular weight cutoff at 8,000 and then placed in 20 mL of PBS solution (10 mM; pH 5.5). The mixture was incubated for 50 h at 37°C with constant horizontal shaking at 100 rpm. At different time points during the incubation, 1 mL aliquot was taken from the solution for ICP analysis of the content of Pt ions.

Colloidal stability assessment

$AuPt_{0.065}$, $AuPt_{0.09}$, or $AuPt_{0.137}$ was diluted to the same concentration in terms of Au mass (10 μg/mL) in deionized water or DMEM containing 10% fetal bovine serum. Then, the solutions were subjected to dynamic light scattering measurement (Malvern, UK) to obtain the hydrodynamic sizes of $AuPt_{0.065}$, $AuPt_{0.09}$, or $AuPt_{0.137}$ at different time points within 14 days.

Quantification of intracellular Au by ICP-MS

Huh-7 cells were seeded in 100-mm cultural dishes and allowed to grow to ~80% confluence and then treated with $AuPt_{0.065}$, $AuPt_{0.09}$, or $AuPt_{0.137}$ of the same concentration in terms of Au mass (5 μg/mL). 12 h later, the cells were washed with PBS twice and then collected by trypsinization for cell counting, followed by precipitation by centrifugation and lysis in 500 μL Aqua regia. The mixtures were sonicated for 5 min and left at RT overnight, with the caps of the tubes tightly sealed. The mixtures were then diluted to 8 mL and filtered through a 0.22 μm filter unit (Millipore Express) for ICP-MS analysis of the Au content.

Subcellular localization detection

Huh-7 cells were seeded in 35-mm cultural dishes with glass bottoms and allowed to adhere and grow for 24 h. The rhodamine B isothiocyanate (RITC)-labeled $AuPt_{0.065}$, $AuPt_{0.09}$, or $AuPt_{0.137}$ was directly added to the culture medium with a final Au concentration of 5 μg/mL. The cells were incubated for 6 h, with 1 μM of LysoGreen (Beyotime) directly added to the culture medium at the last hour of incubation. The cells were then washed with PBS twice before fixation in 4% formaldehyde for 5 min at RT. Subsequently, the cells were stained with 4',6-diamidino-2-phenylindole (DAPI), followed by imaging on an Olympus confocal microscope (OSR, Olympus) using the channels of DAPI, FITC, and Tetramethylrhodamine (TRITC).

Cytotoxicity assay

Huh-7 cells were seeded in a 96-well plate in 100 μL cultural medium at the density of 10,000 cells per well, and allowed to grow for 24 h before any treatment. Afterward, the culture medium was removed, followed by the addition of 100 μL fresh medium containing different concentrations of $AuPt_{0.065}$, $AuPt_{0.09}$, $AuPt_{0.137}$, AuNR, or 3 nm Pt nanoparticles in terms of Au or Pt mass. The cells were incubated for another 24 h and then the medium was replaced with DMEM containing 10% (v/v) CCK8 agent (Boster). To proceed, the cells were further incubated for 2 h before detecting the absorbance at 450 nm in a plate reader (TECAN), with 620 nm as the reference. The viability of cells was calculated as the fraction of the absorbance of treated cells to that of untreated cells.

Apoptosis detection by flow cytometry

Huh-7 cells were seeded in 12-well plates at the density of 100,000 cells per well and allowed to grow for 24 h. Then, the cells were treated with $AuPt_{0.065}$, $AuPt_{0.09}$, or

AuPt$_{0.137}$ of the same concentration in terms of Au mass (10 µg/mL) for 24 h before harvesting for Annexin-V/propidium iodide (PI) duel staining according to the instruction from the manufacturer (Multi Sciences). At least 10,000 cells were recorded for each sample.

TEM imaging of cells
Fixation of cells after different treatments was performed in glutaraldehyde (2.5%) in PBS (100 mM; pH 7.4), followed by postfixation in 1% OsO$_4$ in PBS and gradual dehydration by alcohol and propylene oxide. The fixed cells were embedded in Epon. Next, 60-nm ultrathin sections were cut and placed on a copper meshwork. Finally, the samples were stained with acetate and lead citrate for imaging on a Hitachi H-300 transmission electron microscope.

Western blot
Cells were treated with AuPt$_{0.09}$ (10 µg/mL in terms of Au) for different times and then collected using a cell scraper. The cells were then lysed in cell lysis buffer (Beyotime) containing proteinase inhibitor cocktail (Beyotime) and 10 mM of phenylmethylsulfonyl fluoride (PMSF). The total protein was extracted by centrifugation (15,000 g, 15 min) under 4°C and quantified using the bicinchoninic acid (BCA) kit (Beyotime). 10 µg of each sample was loaded into a 10% SDS-PAGE gel and separated via electrophoresis under 90 V. The separated proteins were transferred onto the 0.22 µM polyvinylidene fluoride (PVDF) membrane (Millipore), followed by sequential staining with primary antibodies (GPX4, ABclonal, A19700; LC3, abcam, ab128025; GAPDH, ABclonal, A19056) and fluorescent secondary antibodies (Alexa Fluor 647 goat anti-rat immunoglobulin G [IgG], BioLegend, 405416). The membrane was then scanned on Odyssey Clx to visualize the proteins. Semi-quantification of the proteins was performed by measuring the integrated intensity of the protein band using ImageJ.

Systemic toxicity evaluation
Animal experiments were performed according to institutional guidelines and were approved by the Institutional Animal Care and Use Committee of Zhejiang University School of Medicine. BALB/c nude mice (6 weeks old, female) were intravenously injected with or without RGD-conjugated AuPt$_{0.09}$ (20 mg/kg in terms of Au mass). The blood samples were collected by orbital bleeding under anesthesia at 1 day or 14 days post-injection. The whole blood was used for hematological analysis and the plasma for blood biochemical analysis. The mice were then sacrificed and the organs, including heart, liver, spleen, lung, and kidney, were collected for hematoxylin and eosin (H&E) staining. To evaluate the long-term toxicity of AuPt$_{0.09}$, the mice were intravenously injected with or without 25 mg/kg of AuPt$_{0.09}$ (in terms of Au) through the tail vein. 30 days later, the mice were sacrificed, and the major organs, including heart, liver, spleen, lung, and kidney, were collected for H&E staining and toxicity evaluation.

Antitumor effects
Animal experiments were performed according to institutional guidelines and were approved by the Institutional Animal Care and Use Committee of Zhejiang University School of Medicine. 5×10^6 Huh-7 cells suspended in 100 µL PBS solution were subcutaneously injected into the flanks of BALB/c nude mice (6 weeks old, female, 5 mice for each group). When the tumors grew to an average size of 100 mm^3, the mice were intratumorally injected with 25 mg/kg (in terms of Au mass) of AuPt$_{0.065}$, AuPt$_{0.09}$, or AuPt$_{0.137}$ twice at a 4-day interval, with PBS as the control. The tumor sizes and the body weights were routinely measured every 4 days, and

the tumor volume was calculated as length × width × width × 0.52. At termination, all the mice were sacrificed and the tumor, heart, liver, spleen, lung, and kidney were collected and weighed, followed by terminal deoxynucleotidyl transferase 2'-deoxyuridine 5'-triphosphate (dUTP) nick end labeling (TUNEL) and/or H&E staining. To evaluate the antitumor effects upon intravenous injection, the tumor-bearing nude mice established as described above were injected with $AuPt_{0.065}$, $AuPt_{0.09}$, or $AuPt_{0.137}$ through the tail vein at a dose of 25 mg/kg (in terms of Au) every 3 days. The tumor sizes and body weights of the mice were measured routinely as described above. The endpoint is defined as death, the tumor burden reaching 1,000 mm^3, or the occurrence of adjacent skin ulcer. The tumors were excised from the mice and weighed at the endpoint.

SUPPLEMENTAL INFORMATION

Supplemental information can be found online at https://doi.org/10.1016/j.xcrp.2021.100538.

AUTHOR CONTRIBUTIONS

D.L. and F.L. conceived and designed the study. X.G., H.L., J.T., and C.Y. performed the experiments. X.G., H.L., and J.T. performed data analysis. X.G., H.L., F.X., W.L., N.W., P.L., B.Z., L.G., and X.H. contributed to writing the manuscript. D.L. and F.L. provided project supervision. All the authors discussed the results and read and approved the final version of the manuscript.

DECLARATION OF INTERESTS

The authors declare no competing interests.

REFERENCES

1. Oleinick, N.L., Morris, R.L., and Belichenko, I. (2002). The role of apoptosis in response to photodynamic therapy: what, where, why, and how. Photochem. Photobiol. Sci. 1, 1–21.

2. Park, W., Cho, S., Han, J., Shin, H., Na, K., Lee, B., and Kim, D.-H. (2017). Advanced smart-photosensitizers for more effective cancer treatment. Biomater. Sci. 6, 79–90.

3. Kim, J., Park, W., Kim, D., Lee, E.S., Lee, D.H., Jeong, S., Park, J.M., and Na, K. (2019). Tumor-specific aptamer-conjugated polymeric photosensitizer for effective endo-laparoscopic photodynamic therapy. Adv. Funct. Mater. 29, 1900084.

4. van Straten, D., Mashayekhi, V., de Bruijn, H.S., Oliveira, S., and Robinson, D.J. (2017). Oncologic photodynamic therapy: basic principles, current clinical status and future directions. Cancers (Basel) 9, 19.

5. Li, X., Lovell, J.F., Yoon, J., and Chen, X. (2020). Clinical development and potential of photothermal and photodynamic therapies for cancer. Nat. Rev. Clin. Oncol. 17, 657–674.

6. Li, Z., Hu, Y., Fu, Q., Liu, Y., Wang, J., Song, J., and Yang, H. (2020). NIR/ROS-responsive black phosphorus QD vesicles as immunoadjuvant

carrier for specific cancer photodynamic immunotherapy. Adv. Funct. Mater. *30*, 1905758.

7. Zhang, Y., Bo, S., Feng, T., Qin, X., Wan, Y., Jiang, S., Li, C., Lin, J., Wang, T., Zhou, X., et al. (2019). A versatile theranostic nanoemulsion for architecture-dependent multimodal imaging and dually augmented photodynamic therapy. Adv. Mater. *31*, e1806444.

8. Wang, C., Xiao, Y., Zhu, W., Chu, J., Xu, J., Zhao, H., Shen, F., Peng, R., and Liu, Z. (2020). Photosensitizer-modified MnO$_2$ nanoparticles to enhance photodynamic treatment of abscesses and boost immune protection for treated mice. Small *16*, e2000589.

9. Rivera-Gil, P., Jimenez de Aberasturi, D., Wulf, V., Pelaz, B., del Pino, P., Zhao, Y., de la Fuente, J.M., Ruiz de Larramendi, I., Rojo, T., Liang, X.-J., and Parak, W.J. (2013). The challenge to relate the physicochemical properties of colloidal nanoparticles to their cytotoxicity. Acc. Chem. Res. *46*, 743–749.

10. Zheng, Z., Liu, H., Zhai, S., Zhang, H., Shan, G., Kwok, R.T.K., Ma, C., Sung, H.H.Y., Williams, I.D., Lam, J.W.Y., et al. (2020). Highly efficient singlet oxygen generation, two-photon photodynamic therapy and melanoma ablation by rationally designed mitochondria-specific near-infrared AIEgens. Chem. Sci. (Camb.) *11*, 2494–2503.

11. Railkar, R., and Agarwal, P.K. (2018). Photodynamic therapy in the treatment of bladder cancer: past challenges and current innovations. Eur. Urol. Focus *4*, 509–511.

12. Lu, C., Zhang, C., Wang, P., Zhao, Y., Yang, Y., Wang, Y., Yuan, H., Qu, S., Zhang, X., Song, G., and Pu, K. (2020). Light-free generation of singlet oxygen through manganese-thiophene nanosystems for pH-responsive chemiluminescence imaging and tumor therapy. Chem *6*, 2314–2334.

13. Wang, C., Cao, F., Ruan, Y., Jia, X., Zhen, W., and Jiang, X. (2019). Specific generation of singlet oxygen through the russell mechanism in hypoxic tumors and GSH depletion by Cu-TCPP nanosheets for cancer therapy. Angew. Chem. Int. Ed. Engl. *58*, 9846–9850.

14. Zhou, Z., Song, J., Tian, R., Yang, Z., Yu, G., Lin, L., Zhang, G., Fan, W., Zhang, F., Niu, G., et al. (2017). Activatable singlet oxygen generation from lipid hydroperoxide nanoparticles for cancer therapy. Angew. Chem. Int. Ed. Engl. *56*, 6492–6496.

15. Vankayala, R., Sagadevan, A., Vijayaraghavan, P., Kuo, C.-L., and Hwang, K.C. (2011). Metal nanoparticles sensitize the formation of singlet oxygen. Angew. Chem. Int. Ed. Engl. *50*, 10640–10644.

16. Chang, Y., Feng, Y., Cheng, Y., Zheng, R., Wu, X., Jian, H., Zhang, D., Tang, Z., Wang, Z., Hao, J., and Zhang, H. (2019). Anisotropic plasmonic metal heterostructures as theranostic nanosystems for near infrared light-activated fluorescence amplification and phototherapy. Adv. Sci. (Weinh.) *6*, 1900158.

17. Long, R., Mao, K., Ye, X., Yan, W., Huang, Y., Wang, J., Fu, Y., Wang, X., Wu, X., Xie, Y., and Xiong, Y. (2013). Surface facet of palladium nanocrystals: a key parameter to the activation of molecular oxygen for organic catalysis and

cancer treatment. J. Am. Chem. Soc. *135*, 3200–3207.

18. Long, R., Mao, K., Gong, M., Zhou, S., Hu, J., Zhi, M., You, Y., Bai, S., Jiang, J., Zhang, Q., et al. (2014). Tunable oxygen activation for catalytic organic oxidation: Schottky junction versus plasmonic effects. Angew. Chem. Int. Ed. Engl. *53*, 3205–3209.

19. Bu, L., Zhang, N., Guo, S., Zhang, X., Li, J., Yao, J., Wu, T., Lu, G., Ma, J.-Y., Su, D., and Huang, X. (2016). Biaxially strained PtPb/Pt core/shell nanoplate boosts oxygen reduction catalysis. Science *354*, 1410–1414.

20. Luo, M., and Guo, S. (2017). Strain-controlled electrocatalysis on multimetallic nanomaterials. Nat. Rev. Mater. *2*, 17059.

21. Wang, L., Zeng, Z., Gao, W., Maxson, T., Raciti, D., Giroux, M., Pan, X., Wang, C., and Greeley, J. (2019). Tunable intrinsic strain in two-dimensional transition metal electrocatalysts. Science *363*, 870–874.

22. Tedsree, K., Li, T., Jones, S., Chan, C.W.A., Yu, K.M.K., Bagot, P.A.J., Marquis, E.A., Smith, G.D.W., and Tsang, S.C.E. (2011). Hydrogen production from formic acid decomposition at room temperature using a Ag-Pd core-shell nanocatalyst. Nat. Nanotechnol. *6*, 302–307.

23. Choi, B.-S., Song, J., Song, M., Goo, B.S., Lee, Y.W., Kim, Y., Yang, H., and Han, S.W. (2019). Core-shell engineering of Pd-Ag bimetallic catalysts for efficient hydrogen production from formic acid decomposition. ACS Catal. *9*, 819–826.

24. Chung, D.Y., Park, S., Lee, H., Kim, H., Chung, Y.-H., Yoo, J.M., Ahn, D., Yu, S.-H., Lee, K.-S., Ahmadi, M., et al. (2020). Activity–stability relationship in Au@Pt nanoparticles for electrocatalysis. ACS Energy Lett. *5*, 2827–2834.

25. Guo, X., Li, X., Kou, S., Yang, X., Hu, X., Ling, D., and Yang, J. (2018). Plasmon-enhanced electrocatalytic hydrogen/oxygen evolution by Pt/Fe–Au nanorods. J. Mater. Chem. A *6*, 7364–7369.

26. Huang, H., Zhang, L., Lv, Z., Long, R., Zhang, C., Lin, Y., Wei, K., Wang, C., Chen, L., Li, Z.-Y., et al. (2016). Unraveling surface plasmon decay in core-shell nanostructures toward broadband light-driven catalytic organic synthesis. J. Am. Chem. Soc. *138*, 6822–6828.

27. Song, Y., Xiang, C., Bi, C., Wu, C., He, H., Du, W., Huang, L., Tian, H., and Xia, H. (2018). pH-Dependent growth of atomic Pd layers on trisoctahedral gold nanoparticles to realize enhanced performance in electrocatalysis and chemical catalysis. Nanoscale *10*, 22302–22311.

28. Bian, T., Zhang, H., Jiang, Y., Jin, C., Wu, J., Yang, H., and Yang, D. (2015). Epitaxial growth of twinned Au-Pt core-shell star-shaped decahedra as highly durable electrocatalysts. Nano Lett. *15*, 7808–7815.

29. Yan, X., Yu, S., Tang, Y., Sun, D., Xu, L., and Xue, C. (2018). Triangular AgAu@Pt core-shell nanoframes with a dendritic Pt shell and enhanced electrocatalytic performance toward the methanol oxidation reaction. Nanoscale *10*, 2231–2235.

30. Rodriguez, J.A., and Goodman, D.W. (1992). The nature of the metal-metal bond in bimetallic surfaces. Science *257*, 897–903.

31. Kitchin, J.R., Nørskov, J.K., Barteau, M.A., and Chen, J.G. (2004). Role of strain and ligand effects in the modification of the electronic and chemical properties of bimetallic surfaces. Phys. Rev. Lett. *93*, 156801.

32. Wang, X., Orikasa, Y., Takesue, Y., Inoue, H., Nakamura, M., Minato, T., Hoshi, N., and Uchimoto, Y. (2013). Quantitating the lattice strain dependence of monolayer Pt shell activity toward oxygen reduction. J. Am. Chem. Soc. *135*, 5938–5941.

33. Jo, D.Y., Lee, M.W., Kim, C.H., Choung, J.W., Ham, H.C., and Lee, K.-Y. (2021). Interplay of ligand and strain effects in CO adsorption on bimetallic Cu/M (M = Ni, Ir, Pd, and Pt) catalysts from first-principles: effect of different facets on catalysis. Catal. Today *359*, 57–64.

34. Hu, X., Saran, A., Hou, S., Wen, T., Ji, Y., Liu, W., Zhang, H., He, W., Yin, J.-J., and Wu, X. (2013). Au@PtAg core/shell nanorods: tailoring enzyme-like activities via alloying. RSC Advances *3*, 6095–6105.

35. He, W., Liu, Y., Yuan, J., Yin, J.J., Wu, X., Hu, X., Zhang, K., Liu, J., Chen, C., Ji, Y., and Guo, Y. (2011). Au@Pt nanostructures as oxidase and peroxidase mimetics for use in immunoassays. Biomaterials *32*, 1139–1147.

36. Zhang, K., Hu, X., Liu, J., Yin, J.-J., Hou, S., Wen, T., He, W., Ji, Y., Guo, Y., Wang, Q., and Wu, X. (2011). Formation of PdPt alloy nanodots on gold nanorods: tuning oxidase-like activities via composition. Langmuir *27*, 2796–2803.

37. Guo, L., Mao, L., Huang, K., and Liu, H. (2017). Pt–Se nanostructures with oxidase-like activity and their application in a selective colorimetric assay for mercury(II). J. Mater. Sci. *52*, 10738–10750.

38. Liu, Y., Wu, H., Li, M., Yin, J.-J., and Nie, Z. (2014). pH dependent catalytic activities of platinum nanoparticles with respect to the decomposition of hydrogen peroxide and scavenging of superoxide and singlet oxygen. Nanoscale *6*, 11904–11910.

39. Mu, X., Wang, J., Li, Y., Xu, F., Long, W., Ouyang, L., Liu, H., Jing, Y., Wang, J., Dai, H., et al. (2019). Redox trimetallic nanozyme with neutral environment preference for brain injury. ACS Nano *13*, 1870–1884.

40. Wen, T., He, W., Chong, Y., Liu, Y., Yin, J.J., and Wu, X. (2015). Exploring environment-dependent effects of Pd nanostructures on reactive oxygen species (ROS) using electron spin resonance (ESR) technique: implications for biomedical applications. Phys. Chem. Chem. Phys. *17*, 24937–24943.

41. Kitchin, J.R., Nørskov, J.K., Barteau, M.A., and Chen, J.G. (2004). Modification of the surface electronic and chemical properties of Pt(111) by subsurface 3d transition metals. J. Chem. Phys. *120*, 10240–10246.

42. Mistry, H., Varela, A.S., Kühl, S., Strasser, P., and Cuenya, B.R. (2016). Nanostructured electrocatalysts with tunable activity and selectivity. Nat. Rev. Mater. *1*, 16009.

43. Shen, X., Liu, W., Gao, X., Lu, Z., Wu, X., and Gao, X. (2015). Mechanisms of oxidase and

superoxide dismutation-like activities of gold, silver, platinum, and palladium, and their alloys: a general way to the activation of molecular oxygen. J. Am. Chem. Soc. *137*, 15882–15891.

44. Chen, Y.-Z., Wang, Z.U., Wang, H., Lu, J., Yu, S.-H., and Jiang, H.-L. (2017). Singlet oxygen-engaged selective photo-oxidation over Pt nanocrystals/porphyrinic MOF: the roles of photothermal effect and Pt electronic state. J. Am. Chem. Soc. *139*, 2035–2044.

45. Li, S., Gu, K., Wang, H., Xu, B., Li, H., Shi, X., Huang, Z., and Liu, H. (2020). Degradable holey palladium nanosheets with highly active 1D nanoholes for synergetic phototherapy of hypoxic tumors. J. Am. Chem. Soc. *142*, 5649–5656.

46. DeRosa, M.C., and Crutchley, R.J. (2002). Photosensitized singlet oxygen and its applications. Coord. Chem. Rev. *233–234*, 351–371.

47. You, Y. (2018). Chemical tools for the generation and detection of singlet oxygen. Org. Biomol. Chem. *16*, 4044–4060.

48. Zhao, M., Liang, Z., Zhang, B., Wang, Q., Lee, J., Li, F., Wang, Q., Ma, D., and Ling, D. (2020). Supramolecular container-mediated surface engineering approach for regulating the biological targeting effect of nanoparticles. Nano Lett. *20*, 7941–7947.

49. Kemker, I., Feiner, R.C., Müller, K.M., and Sewald, N. (2020). Size-dependent cellular uptake of RGD peptides. ChemBioChem *21*, 496–499.

50. Li, M.M., Cao, J., Yang, J.C., Shen, Y.J., Cai, X.L., Chen, Y.W., Qu, C.Y., Zhang, Y., Shen, F., Zhou, M., and Xu, L.M. (2018). Biodistribution and toxicity assessment of intratumorally injected arginine-glycine-aspartic acid peptide conjugated to CdSe/ZnS quantum dots in mice bearing pancreatic neoplasm. Chem. Biol. Interact. *291*, 103–110.

51. Li, M.M., Cao, J., Yang, J.C., Shen, Y.J., Cai, X.L., Chen, Y.W., Qu, C.Y., Zhang, Y., Shen, F., and Xu, L.M. (2017). Effects of arginine-glycine-aspartic acid peptide-conjugated quantum dots-induced photodynamic therapy on pancreatic carcinoma in vivo. Int. J. Nanomedicine *12*, 2769–2779.

52. Desgrosellier, J.S., and Cheresh, D.A. (2010). Integrins in cancer: biological implications and therapeutic opportunities. Nat. Rev. Cancer *10*, 9–22.

53. Suk, J.S., Xu, Q., Kim, N., Hanes, J., and Ensign, L.M. (2016). PEGylation as a strategy for improving nanoparticle-based drug and gene delivery. Adv. Drug Deliv. Rev. *99 (Pt A)*, 28–51.

54. Behzadi, S., Serpooshan, V., Tao, W., Hamaly, M.A., Alkawareek, M.Y., Dreaden, E.C., Brown, D., Alkilany, A.M., Farokhzad, O.C., and Mahmoudi, M. (2017). Cellular uptake of nanoparticles: journey inside the cell. Chem. Soc. Rev. *46*, 4218–4244.

55. Lankveld, D.P.K., Rayavarapu, R.G., Krystek, P., Oomen, A.G., Verharen, H.W., van Leeuwen, T.G., De Jong, W.H., and Manohar, S. (2011). Blood clearance and tissue distribution of PEGylated and non-PEGylated gold nanorods after intravenous administration in rats. Nanomedicine (Lond.) *6*, 339–349.

56. Li, Z., Huang, P., Zhang, X., Lin, J., Yang, S., Liu, B., Gao, F., Xi, P., Ren, Q., and Cui, D. (2010). RGD-conjugated dendrimer-modified gold nanorods for in vivo tumor targeting and photothermal therapy. Mol. Pharm. *7*, 94–104.

57. Sasaki, K., Naohara, H., Cai, Y., Choi, Y.M., Liu, P., Vukmirovic, M.B., Wang, J.X., and Adzic, R.R. (2010). Core-protected platinum monolayer shell high-stability electrocatalysts for fuel-cell cathodes. Angew. Chem. Int. Ed. Engl. *49*, 8602–8607.

58. Gorrini, C., Harris, I.S., and Mak, T.W. (2013). Modulation of oxidative stress as an anticancer strategy. Nat. Rev. Drug Discov. *12*, 931–947.

59. Busbee, B.D., Obare, S.O., and Murphy, C.J. (2003). An improved synthesis of high-aspect-ratio gold nanorods. Adv. Mater. *15*, 414–416.